Designing Coin-Cell Supercapacitors: Combining Graphene Foam with Metal Oxide Composite Electrodes for Improved Energy Storage Performance

Abdulmajid A Mirghni[a], Abubakar Dahiru Shuaibu[a], Yuda Prima Hardianto[a], Fatima Omar AL-Qwairi[a], Arshad Hussain[a], Syed Shaheen Shah[c], Ncholu Manyala[b], Md. Abdul Aziz[a,*]

[a] *Interdisciplinary Research Center for Hydrogen Technologies and Carbon Management (IRC-HTCM), King Fahd University of Petroleum & Minerals, KFUPM Box 5040, Dhahran 31261, Saudi Arabia*

[b] *Department of Physics, University of Pretoria, Pretoria 0002, South Africa*

[c] *Department of Material Chemistry, Graduate School of Engineering, Kyoto University, Nishikyo-ku, Kyoto 615-8520, Japan*

(*) Corresponding author.

E-mail address: maziz@kfupm.edu.sa (Md. A. Aziz)

ABSTRACT

This study presents the development of a high-performance supercapacitor using a sodium cobalt oxide integrated with graphene foam ($NaCoO_2$@GF), PVA-KOH membrane, and activated carbon derived from jute sticks (JC). The $NaCoO_2$@GF/PVA-KOH/JC full-cell device operates effectively across a voltage range of 0 to 1.7 V, demonstrating excellent reversibility and efficient charge storage through diffusion-controlled redox reactions. The device exhibits energy density up to 36.2 Wh kg^{-1} at 0.5 A g-1 and power densitie up to 7749.2 W kg^{-1} at 10 A, as confirmed by GCD data, and shows improved electrochemical performance after stability testing, with enhanced ionic conductivity and electrode material activation. Notably, the $NaCoO_2$@GF/PVA-KOH/JC supercapacitor achieves nearly 100% Coulombic efficiency over 10,000 cycles, maintaining a retention of about 87% for most cycles before a slight drop to 83%. These results demonstrate the superior performance and potential of this composite material for practical energy storage applications.

Keywords: Supercapacitor; Graphene foam; Jute carbon; Sodium cobalt oxide; Hybrid device; Energy storage

1. INTRODUCTION

The rapid progress in energy storage technologies is driven by the increasing demand for high-performance and sustainable power sources [1][2]. Supercapacitors have attracted considerable attention because of their exceptional power density, long cycle life, and fast charge-discharge rates [3][4]. However, achieving high energy density while maintaining excellent power performance remains a significant challenge [5]. Much of the research in this area has focused on developing advanced electrode materials for supercapacitors, driven by the need for more efficient and sustainable energy storage solutions [6]. Also known as electrochemical double-layer capacitors (EDLCs), supercapacitors are emerging as promising energy storage devices due to their ability to provide high power density, rapid charge-discharge cycles, and long cycle life, positioning them as attractive alternatives to traditional batteries and other energy storage technologies [7][8]. The search for innovative electrode materials and architectures is critical to improving the overall performance of supercapacitors. This includes enhancing energy density, power density, and cycling stability [9]. Finding the right balance between high energy density and excellent power and cycling characteristics is crucial for the widespread adoption of supercapacitor technology in various applications [10].

Carbon materials, such as graphene and activated carbon, are highly valued for their excellent conductivity and large surface area, while metal oxides provide superior redox activity and impressive theoretical capacitance. Organic materials, including conductive polymers, offer flexibility and environmental compatibility, making them versatile options for enhancing supercapacitor performance. Also, metal-organic frameworks (MOFs) and their derivatives stand out for their unique structural properties, including high porosity, large surface area, and chemical tunability, further expanding the possibilities for advanced energy storage systems

Sodium cobalt oxide ($NaCoO_2$) has shown promise as a supercapacitor electrode material due to its high theoretical capacitance, excellent electrochemical activity, and stable redox properties

[11]. However, its practical application is often hampered by low electrical conductivity and limited surface area, which limits its overall electrochemical performance. One promising approach to address these limitations is incorporating $NaCoO_2$ into graphene-based architectures [12]. In the compound $NaCoO_2$, sodium is a part of the lattice structure. Sodium's primary role in this context is maintaining the cobalt oxide's structural integrity. However, its presence can also influence the electrochemical properties of the material [12]. In supercapacitors, sodium can contribute to the charge storage mechanism through intercalation processes, where sodium ions move in and out of the lattice during charge and discharge cycles [13]. On the other hand, cobalt oxides are known for their high Pseudocapacitance, which enhances the charge storage capability of the supercapacitor [14]. The cobalt ions in $NaCoO_2$ participate in redox reactions during charge/discharge cycles, significantly boosting the supercapacitor's capacity and energy density. Graphene foam provides excellent electrical conductivity for the active material $NaCoO_2$ to adhere to, improving the efficiency of charge and discharge cycles [15][16]. In summary, Na and Co contribute to the electrochemical properties of the $NaCoO_2$ compound, with Na being part of the structural lattice and Co enhancing Pseudocapacitance. Graphene foam acts as a supportive conductive framework, improving the electrode's electrical conductivity and structural stability.

The polyvinyl alcohol and potassium hydroxide (PVA-KOH) membrane is an electrolyte and a separator in this work. The reason for using this membrane lies in the fact that KOH enhances ionic conductivity by dissociating into potassium ions (K^+) and hydroxide ions (OH^-) in water-based solutions [17]. This increased conductivity is essential for efficient charging and discharging in supercapacitors. Additionally, PVA, a water-attracting polymer, helps maintain the KOH solution and ensures consistent ionic conduction through the membrane. PVA also provides robust mechanical support and flexibility, contributing to the membrane's durability and ability to withstand operational pressures [18]. Its water-attracting nature aids in better wetting, crucial for effective ionic transport and improved interaction between the electrolyte and electrodes, thereby enhancing supercapacitor performance [19]. The PVA/KOH membrane plays a dual role as an electrolyte and a separator: the PVA matrix offers structural support and separation between electrodes, while KOH ensures ionic conductivity [20]. This dual functionality simplifies supercapacitor design and can potentially reduce costs.

Jae Yeon Lee et al. investigated nanostructured cobalt (II, III) oxide in combination with a PVA-KOH gel polymer electrolyte in supercapacitors. Their comparative study included PVA/KOH, urchin-shaped (U–Co_3O_4), and polyhedron-shaped (P–Co_3O_4) cobalt oxides. They measured the ionic conductivity of these samples and found that U–Co_3O_4 exhibited the highest ionic conductivity of 2.61×10^{-2} S cm^{-1} at room temperature. The study highlights that the U–Co_3O_4 surface acts as a conductive network within the polymer matrix, enabling rapid ionic transport. The supercapacitor using U–Co_3O_4 achieved a maximum specific capacitance of 18.2 F g^{-1} at 0.1 A g^{-1} and maintained energy and power densities of 0.5 Wh kg^{-1} and 2.6 kW kg^{-1}, respectively, even at a high a specific current of 5 A g^{-1}. Additionally, the study noted long-term stability with a capacity retention of 84% after 10,000 cycles [21]. However, to the best of our knowledge, the investigation of sodium cobalt oxide integrated with graphene foam composite ($NaCoO_2$/GF) electrodes combined with PVA-KOH as a gel polymer electrolyte in supercapacitors has rarely been reported.

In this study, we conducted hydrothermal synthesis to create $NaCoO_2$ and the $NaCoO_2$@GF composite as positive electrode combined with PVA-KOH gel polymer electrolyte for supercapacitor applications. In this design, the conductive GF network facilitated efficient electron transfer and provided mechanical stability, while the $NaCoO_2$ redox-active material contributed to a high specific capacity. Furthermore, the PVA-KOH gel polymer electrolyte offers a much higher ion conductivity. As a result, when paired with jute sticks derived activated carbon (JC) as the negative electrode and using a PVA-KOH membrane as both electrolyte and separator in a full supercapacitor device configuration, the $NaCoO_2$@GF/PVA-KOH/JC device achieved specific capacity values of 44.8, 39.8, 36.7, 32.5, and 28.1 mAh g^{-1} at 0.5, 1, 2, 5, and 10 A g^{-1}, respectively, operating at an optimized voltage of 1.7 V. Moreover, the $NaCoO_2$@GF/PVA-KOH/JC supercapacitor device demonstrated excellent long-term stability, maintaining nearly 100% Coulombic efficiency and 83% capacity retention after 10,000 continuous charge-discharge cycles. These outstanding electrochemical metrics underscore the potential of the $NaCoO_2$@GF/PVA-KOH/JC supercapacitor device as a promising candidate for future energy storage applications.

2. EXPERIMENTAL

2.1. Materials

All chemicals used in this manuscript were utilized as received without further treatment. Cobalt(II) nitrate hexahydrate ($Co(NO_3)_2 \cdot 6H_2O$), Sodium nitrate ($NaNO_3$), urea, carbon black (CB), polyvinylidene fluoride (PVDF), and N-methyl-2-pyrrolidone (NMP) were procured from Merck, USA. Nickel foam (NF) with a thickness of 0.5 mm (110 PPI) was sourced from the Mini-hua store on AliExpress.com, China. Ethanol, used for cleaning the Ni foam, was also purchased from Merck, USA and used without additional purification. KOH and PVA, used for electrolyte preparation, were similarly obtained from Merck, USA and employed without further modification.

2.2. Synthesis of the materials

For the synthesis of the materials, stoichiometric amounts of $Co(NO_3)_2.6H_2O$ (8.5 g) and $NaNO_3$ (1.5 g) were separately dissolved in 20 ml of deionized (DI) water. The two solutions were then mixed and stirred at room temperature. While stirring, 0.5 g of urea was added dropwise to the mixture. The mixture was left stirring for 2 hours. After 2 hours, the solution was poured into a Teflon-lined autoclave and subjected to a hydrothermal reaction at 160 °C for 8 hours. The solution was then cooled down, washed with DI water several times, and the recovered product was identified as pristine $NaCoO_2$. The same steps were followed for synthesizing the composite but with an optimized GF addition to the mixture (40 mg). The recovered product from this process was identified as the $NaCoO_2$@GF composite. A schematic of the NaCoO2 and NaCoO2@GF materials synthesis steps is shown in Scheme 1. The negative electrode was obtained by using JC as an active material. The details of JC production and full characterization are provided in our previous works [22][23].

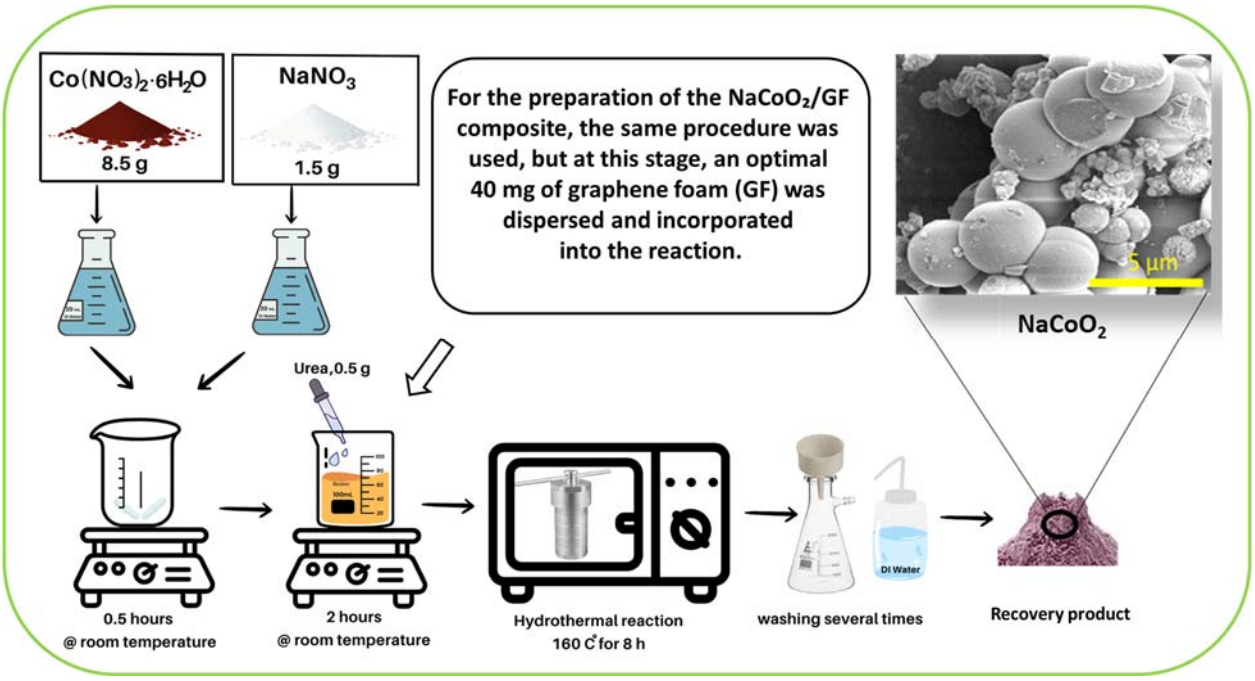

Scheme 1. Schematic illustrating the processes involved in the production of $NaCoO_2$ and $NaCoO_2$@GF materials.

2.3. Synthesis of the electrolyte/separator membrane

A stoichiometric amount of KOH is dissolved in 20 ml of DI water to provide ionic conductivity to the membrane in supercapacitors. PVDF is dissolved in 20 mL of DI water and heated on a hot plate at 80 °C with continuous stirring until fully dissolved. The KOH and PVDF solutions are mixed, poured into a glass Petri dish, and allowed to form a film at room temperature. The film is soaked in 1 M KOH to maintain wettability and ionic conductivity. This method produces a PVDF-KOH membrane with desirable properties, combining effective ionic conductivity with mechanical stability for use in supercapacitors.

2.4. Electrodes fabrication

For the fabrication of the electrodes, a mixture was prepared consisting of 90% of the prepared material (either pristine $NaCoO_2$ or $NaCoO_2$@GF composite), 5% CB as a conductive additive, and 5% PVDF as a binder. NMP was used as the solvent to create the slurry. This slurry was then

coated onto ~1 cm^2 nickel foam current collectors. The coated electrodes were dried overnight at 80 ^oC to ensure complete evaporation of the NMP solvent. The mass loading of the active material on each electrode was adjusted to be 2 mg. The fabricated electrodes were subsequently tested for electrochemical characterization.

2.5. Materials characterization

X-ray diffraction (XRD) analysis was carried out using a Rigaku Miniflex-II diffractometer equipped with Cu-Kα radiation (λ = 0.15416 nm). The instrument was operated at an accelerating voltage of 10 kV and a current of 30 mA. This setup allowed for the precise determination of the crystallographic structure of the samples. X-ray photoelectron spectroscopy (XPS) was performed using a Thermo-Scientific XPS-Microprobe, ESCALAB – 250Xi. This instrument provided detailed information on the elemental composition and chemical states of the surface of the samples. Field emission scanning electron microscopy (FESEM) was conducted using an Oxford Instruments X-Max detector with an accelerating voltage of 2.0 kV. This technique was employed to obtain high-resolution images of the sample morphology and to analyze the surface structure at the micro and nanoscale.

2.6. Electrochemical characterization

Electrochemical characterization was performed using a CHI 760E potentiostat, with measurements conducted in half-cell and full-cell setups. In the half-cell setup, cyclic voltammetry (CV), galvanostatic charge-discharge (GCD), and electrochemical impedance spectroscopy (EIS) were carried out. The configuration included a platinum wire as the counter electrode, an Ag/AgCl electrode saturated with 3 M KCl as the reference electrode, and a $NaCoO_2$@GF composite as the working electrode, all in a 1 M KOH electrolyte. CV measurements were taken at a potential of 0.6 V, GCD measurements at 0.45 V, and EIS measurements at a circuit voltage of 0 V, with a frequency range from 100 Hz to 1 MHz. For the full-cell setup, a coin cell was used to construct the supercapacitor device. The CV and GCD were measured at different potential for the fact that, In CV, the voltage is swept linearly at a constant scan rate, measuring the current response of the supercapacitor. This technique allows for a controlled and gradual change in voltage, often resulting in a wider voltage window without causing significant

overpotentials that might damage the electrode materials or electrolyte. Conversely, the supercapacitor is charged and discharged at a constant current in GCD. This approach can induce higher overpotentials, especially at the voltage range limits, leading to a reduced voltage window to prevent overloading and ensure the stability of the supercapacitor. The $NaCoO_2$@GF composite served as the positive electrode, JC as the negative electrode, and KOH@PVA as the gel electrolyte. This supercapacitor device operated within a cell potential range of 0 to 1.7 V.

The below equation (1) is applied for the computing of specific capacitance (F g^{-1}) [24].

$$C_S = \frac{i \int V \Delta t}{m V^2} \quad (1)$$

In the given expression, Δt denotes the discharging time, I_d refers to the specific current and can be expressed as $I_d = i/m$.

In the full asymmetric supercapacitor, a charge balance is necessary due to the different performances of $NaCoO_2$@GF and JC. To ensure equal charge amounts in the negative and positive electrodes, equation (2) was applied [15].

$$\frac{m_{(+)}}{m_{(-)}} = \frac{C_{S(-)} \Delta v_{(-)}}{C_{S(+)} \Delta v_{(+)}} \quad (2)$$

The symbols $m(+)$ and $m(-)$ denote the active masses of the positive and negative electrodes, while $C_{S(+)}$ and $C_{S(-)}$ signify the specific capacitance values of the positive and negative electrodes, respectively. Additionally, the OPWs of the positive electrode are denoted by $\Delta v_{(+)}$ and the negative electrode by $\Delta v_{(-)}$.

In a coin cell arrangement, an asymmetrical cell was constructed with $NaCoO_2$@GF serving as the positive electrode and JC as the negative electrode. The electrolyte in this system was 1 M KOH@PVA, and the filter paper served as a separator. The supercapacitor's performance can be evaluated based on two essential factors: specific energy (Ed) and specific power (Pd). Equations (3) and (4) were used to calculate the Ed and Pd of the asymmetric supercapacitor device [24].

$$E_d = \frac{i}{3.6m} \int V dt \quad (3)$$

$$P_d = 3600\frac{E_d}{\Delta t} \quad (4)$$

Where i (mA) signifies current, m (mg) denotes active mass, Δt (s) represents discharge time and $\int Vdt$ denotes the area under the curve of the supercapacitor's discharge time.

3. RESULTS AND DISCUSSION

3.1. Structure, textural analysis, surface chemistry and morphology

Fig. 1(a) presents the XRD pattern of bare $NaCoO_2$, measured within the 2θ range of 10° to 80°, with the intensity being appropriately recorded. The pattern was analyzed using the Joint Committee on Powder Diffraction Standards (JCPDS) No. 87-0274 and corresponds to a monoclinic unit cell with space group C2/m, utilizing the Visualization Molecular Structure Diamond Crystal (VMSD) software. All observed peaks are consistent with the JCPDS No. 87-0274, confirming the chemical formula $NaCoO_2$ [25]. The crystal system is monoclinic with cell parameters a_m = 4.8996(6) Å, b_m = 2.8263(2) Å, c_m = 5.7156(5) Å, and β = 106.069(6)°. The XRD pattern displays sharp and narrow peaks, indicative of the high crystallinity of the synthesized material [26]. Specific peaks were observed at 2θ values of 14.5°, 17.2°, 23.9°, 34.5°, 41.5°, 59.2°, and 67.3°, corresponding to the (hkl) reflection planes (001), (002), (004), (100), (103), (106), and (110), respectively. All these peaks are indexed according to JCPDS No. 87-0274. Fig. 1(b) compares the XRD patterns of bare $NaCoO_2$ and the $NaCoO_2$@GF composite. The $NaCoO_2$@GF composite pattern (blue) shows a similar spectra to the $NaCoO_2$ (orange), confirming the structural consistency of $NaCoO_2$ in the composite. However, an additional peak at 2θ = 33.5° is observed in the $NaCoO_2$@GF composite, attributed to the presence of carbon, thus confirming the incorporation of graphene foam (GF) into the composite.

Fig. 1(b) presents the BJH pore size distribution and N_2 adsorption-desorption isotherms for $NaCoO_2$ and $NaCoO_2$@GF, providing valuable information about the porous structure and surface characteristics of these materials. The N_2 adsorption-desorption isotherms for both $NaCoO_2$ and $NaCoO_2$@GF exhibit Type-3 behavior. The presence of an H3 hysteresis loop indicates that the materials possess mesopores (pore sizes between 2 nm and 50 nm). H3 hysteresis loops are often associated with materials that exhibit slit-shaped pores, which can be attributed to the

mesoporous nature and irregular pore structure of the materials [ref]. The BJH pore size distribution reveals that the majority of pores fall within the mesopore range, specifically between 2 nm and 35 nm for both $NaCoO_2$ and $NaCoO_2$@GF. This indicates that both materials primarily consist of mesopores. However, an important feature in the BJH graph is the presence of a peak at lower pore diameters, suggesting the existence of minor micropores. This is particularly evident for the $NaCoO_2$@GF composite, indicating that the introduction of graphene foam (GF) plays a role in generating a considerable micropores in the material [ref]. These smaller pores could result from the interaction between $NaCoO_2$ and the graphene foam during the synthesis process. The $NaCoO_2$@GF composite shows a notably higher nitrogen adsorption at high relative pressure, which reflects an increased surface area and porosity compared to $NaCoO_2$ alone. This suggests that the graphene foam enhances the porous structure of $NaCoO_2$ by providing additional surface area for nitrogen adsorption, particularly at higher relative pressures, a characteristic often associated with mesoporous materials. The significant increase in nitrogen uptake at high relative pressure for the $NaCoO_2$@GF composite is indicative of a larger number of mesopores and possibly macropores, contributing to improved overall porosity. The specific surface area of NaCoO2@GF is reported to be 28 $m^2 g^{-1}$, a considerable increase from the 9.8 $m^2 g^{-1}$ for $NaCoO_2$ alone. This increase in surface area is a direct result of the incorporation of graphene foam, which likely introduces additional pore volume and surface area for adsorption [ref]. The improved surface area and enhanced porosity of $NaCoO_2$@GF, as evidenced by the BJH analysis and N_2 adsorption isotherms, directly contribute to an improved electrochemical performance of the composite. The increased surface area provides more active sites for charge storage, while the enhanced porosity can facilitate better ion diffusion and electron transport.

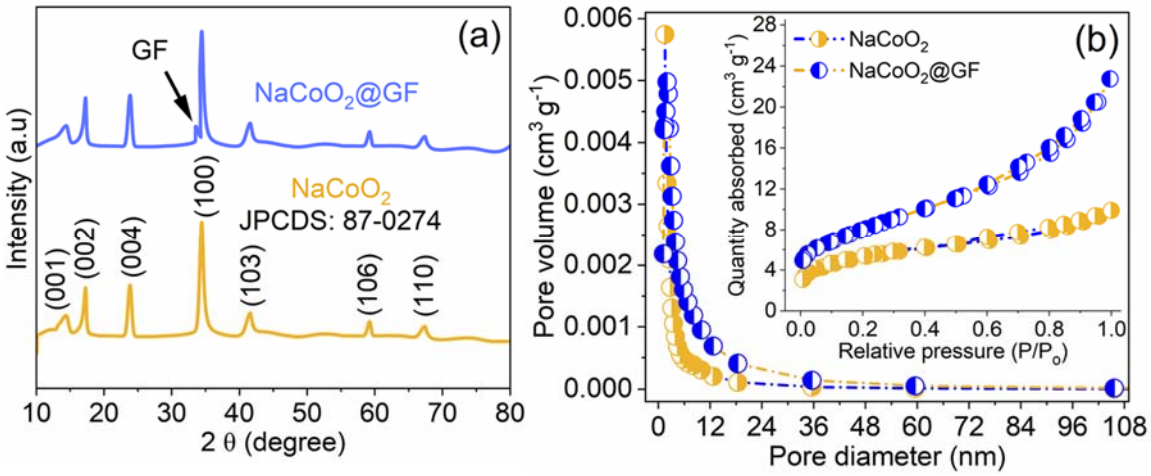

Fig. 1. (a) XRD patterns and (b) BJH plot associated with N_2-ithotherm as inset of $NaCoO_2$ and $NaCoO_2$@GF composite

The XPS survey spectrum of $NaCoO_2$, as shown in Fig. 1(a), highlights the presence of the main elements in the sample. The prominent peaks correspond to Na 1s core level peak, Co 2p: core level peaks and O 1s core level peak. These peaks are characteristic of the $NaCoO_2$ compound, confirming its elemental composition and purity. The XPS survey spectrum of the composite sample $NaCoO_2$@GF, shown in Fig. 1(b), reveals additional features compared to the $NaCoO_2$ sample. In addition to the peaks observed in $NaCoO_2$, the composite sample shows C 1s extra peak corresponding to the carbon 1s core level. This peak is attributed to the presence of GF in the composite, indicating the successful incorporation of GF into the $NaCoO_2$ matrix. The presence of the C 1s peak in the composite sample indicates the integration of graphene, which is known for its excellent electrical conductivity. The addition of GF to the $NaCoO_2$ matrix enhances the overall electrical conductivity of the composite sample. This improvement is due to the conductive pathways provided by the graphene, which facilitate better electron transport throughout the material.

In Fig. 2(c), the high-resolution emission XPS spectra of the Na 1s core level in the $NaCoO_2$ sample reveal two distinct peaks at binding energies of 1072.7 eV, which is attributed to the Na 1s core level and 1074.8 eV at a slightly higher binding energy suggests a different chemical state of sodium within the $NaCoO_2$ matrix [27]. These two peaks indicate that sodium exists in two

different environments within the $NaCoO_2$ structure [28]. In Fig. 1(d), the high-resolution emission XPS spectrum of the Co 2p core level provides detailed insights into the cobalt chemical states within the $NaCoO_2$ and $NaCoO_2$@GF samples. The Co 2p spectrum is characterized by several peaks: Co $2p_{3/2}$ at 782.1 eV and 787.8 eV peaks correspond to the Co $2p_{3/2}$ spin-orbit components. The binding energy at 782.1 eV is typical for Co^{2+} in a cobalt oxide environment, while the peak at 787.8 eV may be associated with satellite structures often seen in Co^{2+} compounds. Co $2p_{1/2}$ at 797.9 eV and 804.2 eV peaks correspond to the Co $2p_{1/2}$ spin-orbit components. The binding energy at 797.9 eV is indicative of Co^{3+}, and the peak at 804.2 eV is also associated with Co^{3+} or satellite peaks. The analysis of these peaks suggests that cobalt exists in both Co^{2+} and Co^{3+} oxidation states within the $NaCoO_2$ and $NaCoO_2$@GF samples. The presence of both oxidation states is critical for understanding the electronic structure and catalytic properties of the material [29][30]. In Fig. 2(e), the core level spectrum of the O 1s in the $NaCoO_2$ sample shows two fitted peaks at binding energies 532.9 eV, attributed to the O 1s core level in Co-O bonds and 534.7 eV, associated with Na-O bonds. The presence of these two peaks confirms the different chemical states of oxygen in the $NaCoO_2$ sample, corresponding to its interactions with cobalt and sodium atoms [31]. Fig. 1(f) presents the C 1s spectrum of the $NaCoO_2$@GF composite, showing multiple peaks at different binding energies: 287.2 eV (Sp^2, C=C), corresponds to sp^2-hybridized carbon atoms (C=C) in the graphene component, 289.4 eV (C=O), associated with carbon-oxygen double bonds (C=O), 281.2 eV (C-O-C), attributed to carbon-oxygen single bonds in an ether linkage (C-O-C), 292.7 eV (O-C=O), corresponds to carboxyl groups (O-C=O), and 294.6 eV (π-π*), associated with π-π electron transitions or satellite peaks, characteristic of the electronic structure of graphene [32]. The presence of sp^2 carbon (C=C) from graphene is critical for enhancing the electrical conductivity of the $NaCoO_2$@GF composite. The conductive pathways provided by graphene improve the overall electronic properties of the material. Moreover, the various oxygen-containing functional groups (C=O, C-O-C, O-C=O) in the composite may influence its chemical reactivity, stability, and potential applications in energy storage [33].

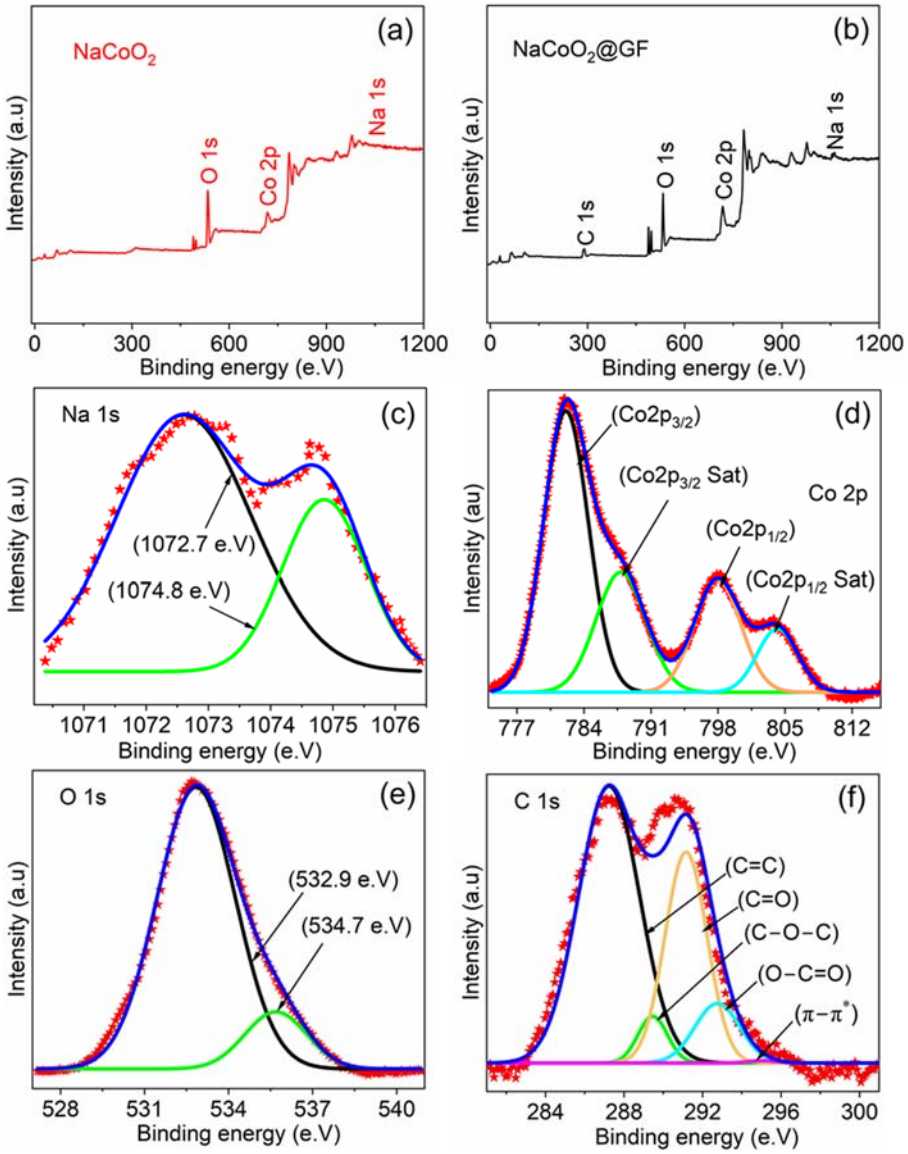

Fig. 2. (a,b) wide XPS survey spectra of $NaCoO_2$ and $NaCoO_2$@GF, respectively, high-resolution spectra of (c) Na 1s, (d) Co 2p, (e) O 1s for $NaCoO_2$ and (f) C 1s for $NaCoO_2$@GF composite

The SEM micrographs of the $NaCoO_2$ samples (Fig. 3(a) and 3(b)) display a spherical morphology with small secondary species distributed within the spheres. The average size of these spheres is approximately 350 nm. The low magnification image of $NaCoO_2$@GF in Fig. 1(c) depicts the composite structure, where $NaCoO_2$ particles are combined with GF. High magnification in Fig. 1(d) does not reveal significant morphological changes in the $NaCoO_2$ spheres due to the presence of GF, indicating that incorporating GF does not alter the fundamental spherical structure of $NaCoO_2$. GF is not visible in the SEM images, likely because it was coated on the

surface of $NaCoO_2$ spheres and dispersed through ultrasonication for several hours, making it difficult to distinguish in the SEM images [32]. Despite the inability to visualize GF in the SEM images, XPS analysis confirms the presence of high-quality graphene foam on the surface of $NaCoO_2$ spheres, suggesting the successful integration of GF into the composite material. The stable spherical morphology of $NaCoO_2$ in the presence of GF indicates that the structural integrity of the particles is maintained. The SEM and XPS analyses provide a comprehensive understanding of the $NaCoO_2$@GF composite. While SEM shows the morphological details, XPS confirms the successful incorporation of graphene foam, highlighting the synergistic benefits of the composite material.

The micrographs of $NaCoO_2$, further confirmed by HRTEM, are shown in Fig. 3(e). In agreement with the SEM results in Figs. 3(a) and 3(b), the HRTEM reveals spherical morphologies with an average diameter of 350 nm. Figs. 3(f) and 3(g) display the HRTEM images of $NaCoO_2$@GF at high magnifications of 50 nm and 20 nm, respectively. In these figures, a clear integration of GF into $NaCoO_2$ is observed, with GF sheets and $NaCoO_2$ particles attached together. This integration is evident at a high resolution of 50 nm and becomes even clearer at 20 nm, as shown in Figs. 3(f) and 3(g). Such close attachment of GF to $NaCoO_2$ is necessary to provide a surface for effective charge mobility and storage, while also evidencing the sheet-like morphology of GF. The lattice fringes of $NaCoO_2$@GF and the d-spacing become visible at a magnification of 10 nm (Fig. 3(h)), indicating a high degree of crystallinity in the composite material. The selected area electron diffraction (SAED) pattern is shown in Fig. 3(i). The SAED pattern exhibits distinct diffraction spots (rings), portraying the polycrystalline nature of the material, which is consistent with the XRD results in Fig 1.

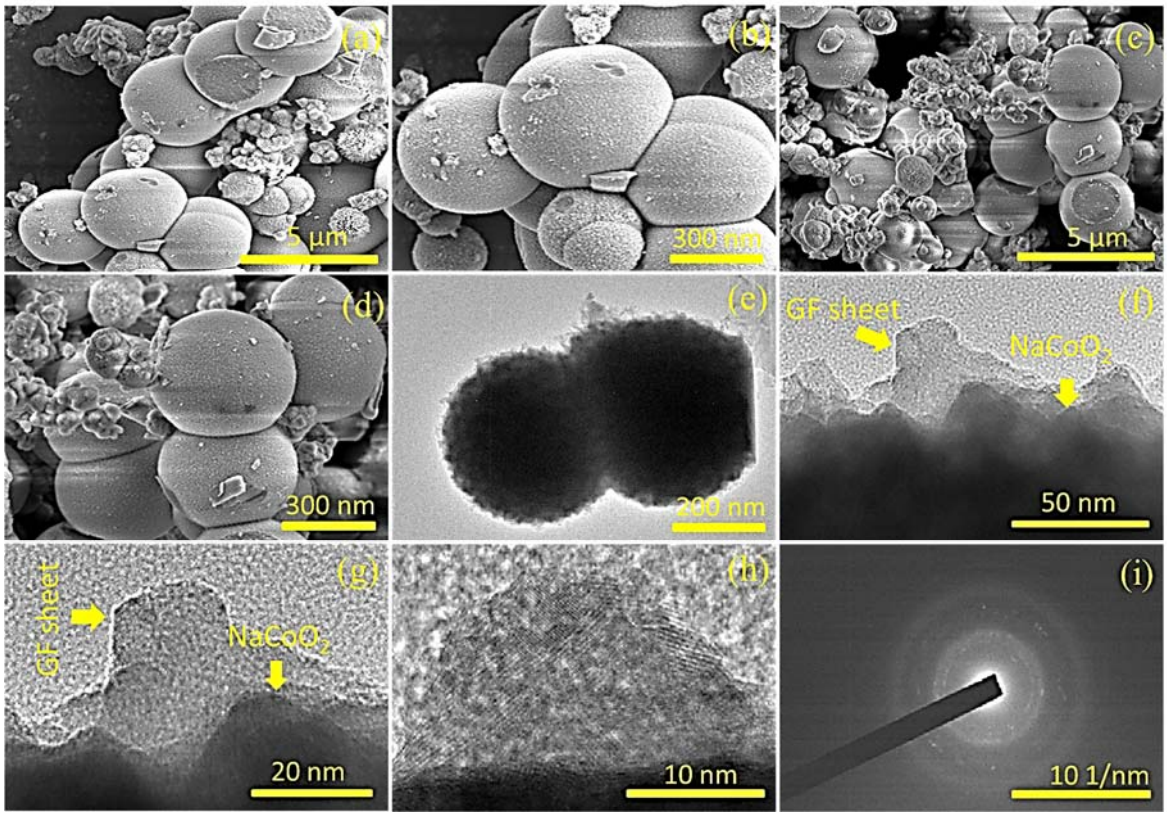

Fig. 3. (a, b) Low and high magnification FESEM images of $NaCoO_2$, respectively; (c, d) Low and high magnification FESEM images of $NaCoO_2$@GF, respectively; (e) HRTEM image of the as-prepared $NaCoO_2$ sample; (f, g, h, i) HRTEM images and corresponding selected area electron diffraction (SAED) pattern of $NaCoO_2$@GF.

3.2. Electrochemistry

3.2.1. Half-cell configuration

Fig. 4 (a,b) presents the electrochemical characterization of bare nickel foam (Bare NF), $NaCoO_2$, and $NaCoO_2$@GF composites in a half-cell setup. Fig. 4(a) shows the cyclic voltammetry (CV) curve of Bare NF at a scan rate of 50 mV s^{-1} within a potential window of 0.0–0.6 V. A pair of redox peaks is observed, with an anodic peak around 0.32 V and a cathodic peak around 0.41 V, confirming the faradic behavior of the Ni foam. Fig. 4(b) displays the CV profiles of the materials, measured at a scan rate of 50 mV s^{-1} within the same potential range of 0.0–0.6 V vs. Ag/AgCl.

The Bare NF shows a negligible current response, with minimal contribution compared to $NaCoO_2$ and $NaCoO_2$@GF. In contrast, both $NaCoO_2$ and $NaCoO_2$@GF exhibit pseudocapacitive behavior, displaying distinct redox peaks. Specifically, the CV curves show two redox peaks in the 0.1–0.2 V and 0.4–0.5 V ranges, which are attributed to fast and reversible Co^{2+}/Co^{3+} redox reactions. Notably, the $NaCoO_2$@GF composite demonstrates a larger enclosed CV area than $NaCoO_2$, indicating superior capacitive behavior. This increased area suggests improved conductivity and ion diffusion properties attributed to the synergy between $NaCoO_2$ and the graphene form (GF) framework. The GF forms a conductive network, facilitating faster electron transport and better ion diffusion [34]. Additionally, the GF enhances electrolyte ion accessibility and penetration into the active material, reducing interfacial resistance and promoting ion diffusion [35]. Consequently, the $NaCoO_2$@GF composite demonstrates a significantly broader CV profile compared to the bare $NaCoO_2$ material, indicating enhanced electrochemical performance. Fig. 4(c) compares the GCD profiles of $NaCoO_2$ and $NaCoO_2$@GF measured at a specific current of 1 A g^{-1} and a potential range of 0 to 0.45 V vs. Ag/AgCl. The $NaCoO_2$@GF composite displays longer charge and discharge times compared to the bare $NaCoO_2$ material. The longer charge and discharge times for the $NaCoO_2$@GF composite suggest a higher specific capacity compared to the bare $NaCoO_2$.This behavior observed in the GCD profiles is consistent with the enhanced capacity behavior indicated by the larger enclosed area in the CV profiles of $NaCoO_2$@GF shown in Fig. 4(b).

Fig. 4(d) illustrates the Nyquist plots along with the corresponding fitting curves obtained from the EIS analysis of $NaCoO_2$ and $NaCoO_2$@GF. These fitting curves were generated by minimizing the root mean square error between the experimental total impedance and the simulated total impedance produced by the proposed electrical circuit model depicted in Fig. 4(e). This model operates on the principle that ions first navigate through the bulk electrolyte region, represented by R_s, before proceeding through the porous structure to reach the active material. Within the porous structure, ion movement can occur via two mechanisms: the formation of an electrochemical double layer, indicated by CPE_p, or through a resistive pathway, denoted as R_p. Once the ions arrive at the active material, they can interact in two distinct ways: forming an

electrochemical double layer at the active material surface, represented as CPE_c, or encountering charge transfer resistance, captured by R_{ct} and CPE_{ct}.

These interactions and mechanisms can be quantitatively analyzed, leading to a mathematical representation of the impedance. Generally, the impedance of the constant phase element can be expressed using the following equation [36]:

$$Z_{CPE} = \frac{1}{Q(i\omega)^n} \quad (5)$$

In equation (5), the parameter Q represents a constant associated with the constant phase element, and the exponent n indicates its exponential factor. The possible values for n range from 0.5 to 1. A higher Q value indicates a greater ability of the constant phase element to store energy. The value of n describes the nature of this energy storage: values near 0.5 suggest a diffusive mechanism, whereas values close to 1 indicate a capacitive mechanism.

Using equation (5) and the typical electrical circuit analysis, the total impedance of the electrical circuit model illustrated in Fig. 4(e), which represents the entire mechanism within the electrode, can be expressed as follows:

$$Z = R_s + \left(\frac{R_{ct}Z_{CPE_c} + Z_{CPE_{ct}}Z_{CPE_c}}{R_{ct} + Z_{CPE_{ct}} + Z_{CPE_c}}\right) + \left(\frac{R_p Z_{CPE_p}}{R_p + Z_{CPE_p}}\right) \quad (6)$$

Numerically, the fitting was performed using the Solver function in Microsoft Excel, aiming to minimize the root mean square error between the experimental total impedance and the simulated total impedance. Notably, this fitting procedure achieved a maximum average error of 2.5%, demonstrating the reliability of both the proposed model and the fitting technique. The parameters obtained from this fitting process are detailed in Table 1.

Table 1. Extracted parameters of the electrical circuit model fitting

Electrode	R_s (Ohm)	R_{ct} (Ohm)	R_p (Ohm)	n_{ct}	n_c	n_p
$NaCoO_2$	2.2	1.4	9.7	0.99	0.68	0.68
$NaCoO_2$@GF	1.5	0.36	8.8	0.99	0.72	0.72

Interestingly, the $NaCoO_2$@GF electrode demonstrates a lower resistance (R_p) compared to the $NaCoO_2$ electrode, which suggests that the porous structure of $NaCoO_2$@GF facilitates enhanced ionic transport. In addition to the improvement in ionic conductivity within the porous structure region, the reduced charge transfer resistance (R_{ct}) of the $NaCoO_2$@GF electrode further signifies its superior electrochemical performance relative to $NaCoO_2$. These findings are supported by the extracted exponential constant (n) for all constant phase elements in the electrical circuit model, which provide valuable insights into the modified electrode's behavior. Remarkably, the incorporation of graphene foam into the $NaCoO_2$ structure leads to an increase in these exponential values, approaching 0.75. This change indicates a significant transition in the electrochemical behavior of the electrode, shifting towards a combination of diffusive and capacitive mechanisms, thereby enhancing overall electrochemical performance of the electrode.

Fig. 4(f) shows the CV profiles of the $NaCoO_2$@GF composite measured at various scan rates ranging from 10 to 75 mV s^{-1}. As the scan rate increases, the redox peaks in the CV profiles shift slightly, indicating a combination of capacitive and diffusion-controlled charge storage mechanisms in the $NaCoO_2$@GF composite. The GCD profiles of the $NaCoO_2$@GF composite were obtained at different specific currents ranging from 0.5 to 5 A g^{-1}, as illustrated in Fig. 4(g). The longer charge and discharge times observed at lower specific currents suggest a higher specific capacitance for the $NaCoO_2$@GF composite. The decreasing discharge time at higher specific currents indicates better rate capability of the $NaCoO_2$@GF composite. The storage mechanisms observed in the CV and GCD analyses are in good agreement, confirming the combination of capacitive and diffusion-controlled charge storage characteristics in the $NaCoO_2$@GF composite. Furthermore, the bar chart in Fig. 4(h) illustrates the specific capacitance values of $NaCoO_2$ and $NaCoO_2$@GF at specific currents of 0.5, 1, 2, 3, and 5 A g^{-1}. $NaCoO_2$ shows specific capacitance values of 232, 216, 196, 111, and 65 F g^{-1}, respectively, while $NaCoO_2$@GF exhibits significantly higher values of 437, 357, 325, 288, and 84 F g^{-1} at the same specific currents. This higher specific capacitance of $NaCoO_2$@GF compared to the bare $NaCoO_2$ material confirms the enhanced electrochemical performance of the composite.

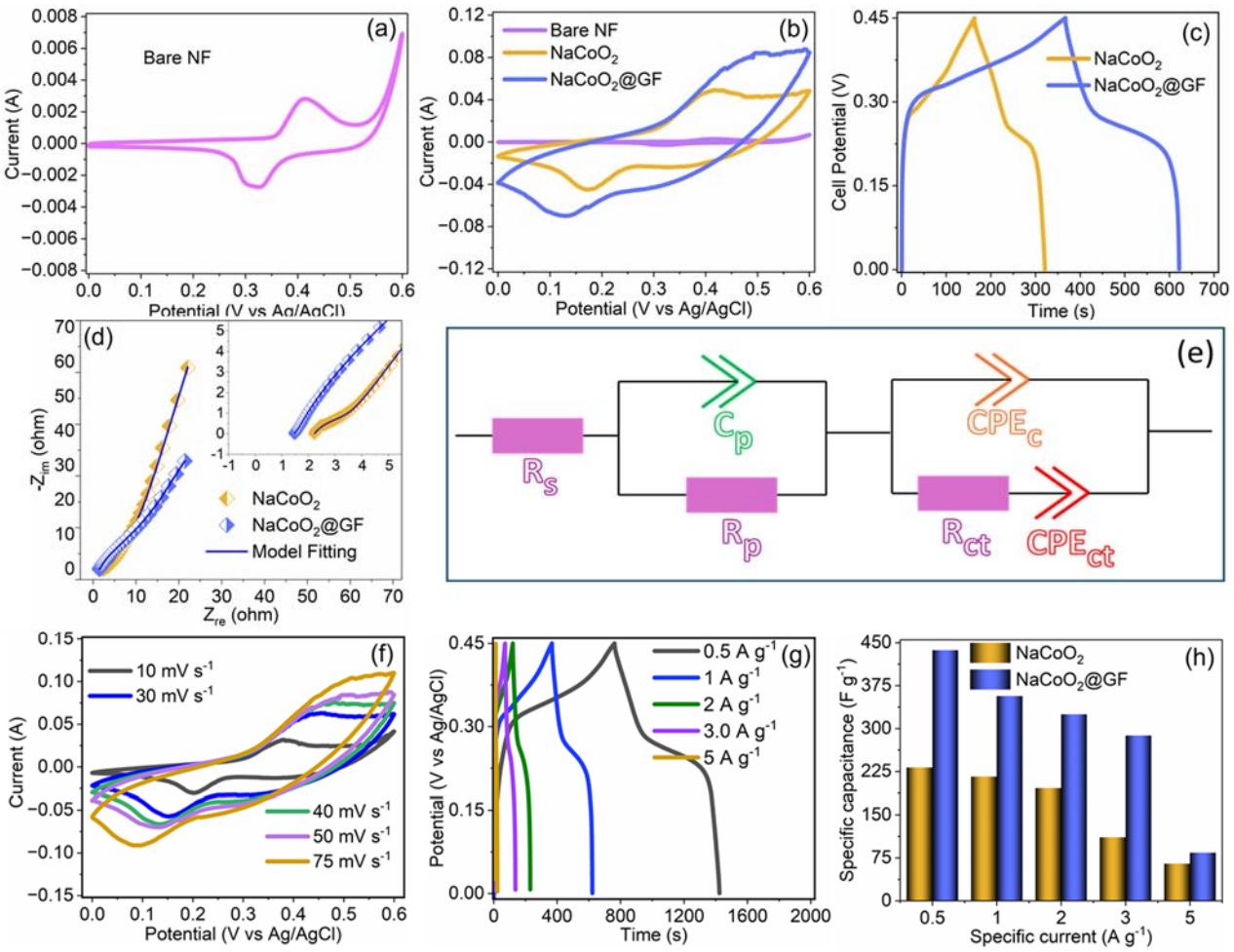

Fig. 4. Electrochemical characterization of bar nickel foam (Bare NF), $NaCoO_2$ and $NaCoO_2$@GF composite electrodes in 3-electrode setup: (a) CV profile of Bare NF and (b) CV profiles of Bare NF, $NaCoO_2$ and $NaCoO_2$@GF at 50 mV s^{-1}, (c) GCD profiles of $NaCoO_2$ and $NaCoO_2$@GF at a specific current of 1 A g^{-1}, (d) Experimental and model fitting EIS of $NaCoO_2$ and $NaCoO_2$@GF, and (e) Equivalent circuit used for fitting the EIS data in (d), (f) CV profiles of $NaCoO_2$@GF at different scan rates and (g) GCD profiles of $NaCoO_2$@GF at different specific currents and (h) specific capacity versus specific current calculated for $NaCoO_2$ and $NaCoO_2$@GF

To reinforce the earlier findings regarding the energy storage mechanism of the $NaCoO_2$@GF, analyzing CV at different scan rates can provide valuable insights into the reversibility of the device's energy storage process. The Power rule analysis and Dunn method are two typical methods used to analyze CV at different scan rates.

Based on the power rule analysis, the peak current (i_p) values derived from at various scan rates can be represented as a function of the scan rate. This relationship is described in equation (7) [37].

$$i_p = av^b \quad (7)$$

Equation (8) involves several variables: the peak current at the CV peak, denoted as i_p, the scan rate represented by *v, a is a* constant, and *b* pertains to the electrochemical mechanism. Generally, a *b* value close to 1 indicates that the electrode exhibits predominantly capacitive behavior, whereas a *b* value near to 0.5 suggests a more diffusive behavior. Notably, the anodic peak (positive scan rate) and cathodic peak (negative scan rate) have b values of 0.7 and 0.62, respectively, as shown in Fig. 5(a). These values are similar, implying that the energy storage mechanisms during charging (anodic) and discharging (cathodic) are almost reversible. This reversible characteristic is beneficial for the performance of electrochemical properties.

To further assess the proportions of capacitive and diffusive contributions to the energy storage mechanism of the $NaCoO_2$@GF electrode material, the CV data at various scan rates is analyzed using the Dunn method. This approach allows the peak current derived from the CV data to be represented as a combination of the capacitive component (k_1v) and the diffusive component ($k_2v^{1/2}$), as detailed in the following equation [38].

$$i_p = k_1 v + k_2 v^{1/2} \quad (8)$$

Equation (8) shows that the peak current in the CV data is the sum of two components: a capacitive contribution, represented by the constant k_1 multiplied by the scan rate *v*, and a diffusive contribution, represented by the constant k_2 multiplied by the square root of the scan rate *v*. Figure 5(b) presents the results from the Dunn method, revealing that $NaCoO_2$@GF exhibits a notable diffusive contribution, starting at 82% at a scan rate of 10 mV s^{-1} and decreasing to 62% at 75 mV s^{-1}. This trend, where the diffusive contribution decreases with increasing scan rate, is typical as the capacitive contribution becomes more dominant at higher scan rates. Additionally, Figure 5(c) illustrates the energy storage mechanism, showing that at a scan rate of 50 mV s^{-1}, 66% of the area under the CV curve is attributed to the diffusive contribution.

Figure 5(d) presents a stability test of $NaCoO_2$@GF, evaluated over 4000 cycles of continuous GCD at 10 A g^{-1}. The double Y plot shows that the electrode material maintains a high coulombic efficiency of approximately 99% after 4000 cycles, demonstrating its excellent charge-discharge reversibility. Furthermore, the material retains 96% of its capacitance, indicating strong electrochemical stability over extended cycling. This remarkable stability is attributed to the high degree of crystallinity of $NaCoO_2$ and the addition of graphene foam (GF), which enhances the mechanical strength of the composite and contributes to its durability during cycling.

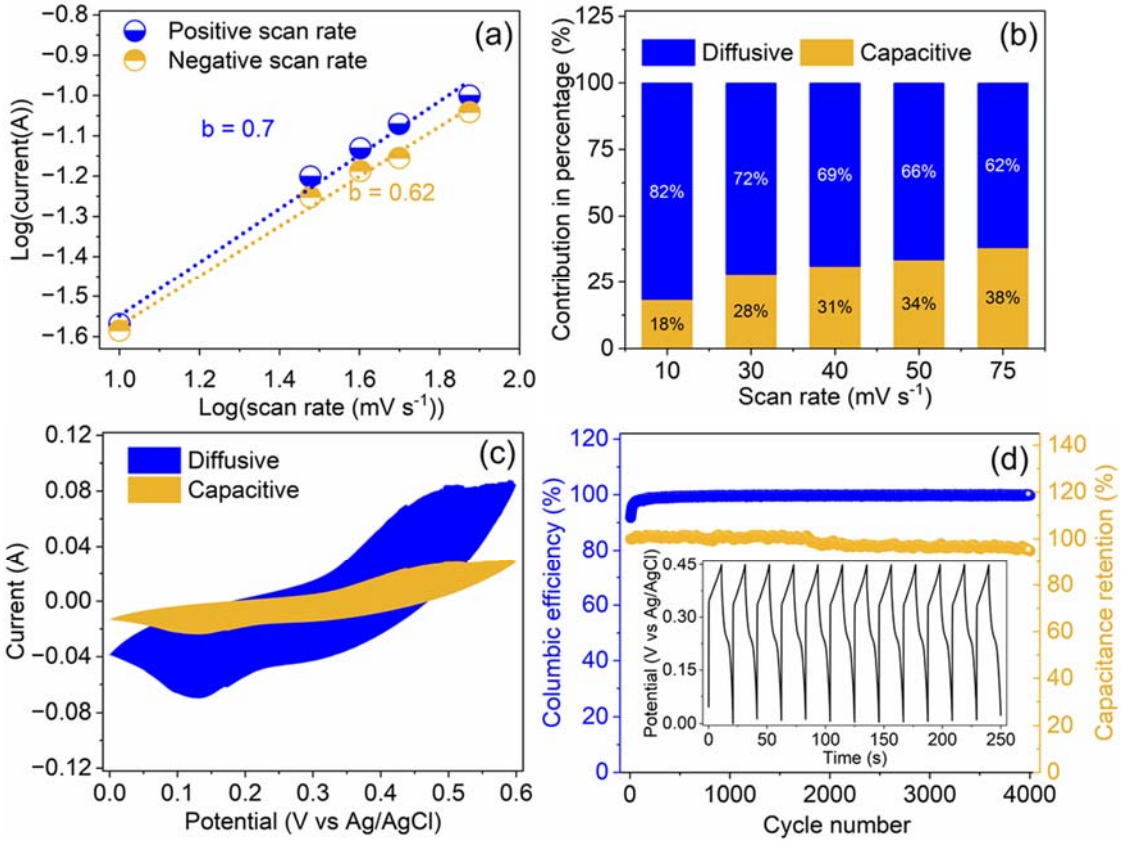

Fig. 5. (a) Power law analysis of $NaCoO_2$@GF, (b) Proportional contributions of capacitive and diffusive mechanisms in the CV at varying scan rates for $NaCoO_2$@GF, (c) CV curve of $NaCoO_2$@GF at 50 mV s^{-1}, showing 66% of the area attributed to the diffusive mechanism, and (d) Stability test of $NaCoO_2$@GF conducted at 10 A g^{-1}.

3.2.2. Full-cell configuration

$NaCoO_2$@GF operates best between 0 and 0.6 V vs. Ag/AgCl, while JC functions optimally between -1.1 and 0 V vs Ag/AgCl. This suggests a total cell potential range of 0 to 1.7 V for the supercapacitor asymmetric device, as seen in Fig. 6(a). Fig. 6(b, c) presents the voltage optimization results for the $NaCoO_2$@GF/PVA-KOH/JC supercapacitor. The device was tested at varying voltages of 1.4, 1.55, 1.6, and 1.7 V at a scan rate of 50 mV s^{-1}. The data shows that the supercapacitor operates most effectively at 1.7 V, as indicated by the appearance of a small oxidation peak at this voltage. This peak suggests that the device begins to experience voltage-induced degradation beyond 1.7 V, making it the optimal voltage for stable operation. The galvanostatic charge-discharge (GCD) profiles in Fig. 6(b) further support this, confirming that the device functions best within this voltage range. The CV profiles for the full-cell device, displayed in Fig. 6(d), were recorded at scan rates ranging from 10 to 100 mV s^{-1}. The tests used a PVA/KOH membrane soaked in 1 M KOH, serving as the electrolyte and separator. The device operated efficiently across the potential range of 0 to 1.7 V, aligning with the optimal ranges identified for the individual electrode materials. The full-cell CV profiles feature two broad redox peaks at approximately 0.81 V and 1.28 V. These peaks indicate the diffusion-controlled reversible redox reaction of $Co^{2+} \leftrightarrow Co^{3+}$, which suggests charge storage through surface redox reactions. Despite the increase in scan rate from 10 to 100 mV s^{-1}, the shape of the CV profiles remained consistent while the current response increased. This behavior indicates good reversibility of the electrode materials. Fig. 6(e) shows the GCD profiles for the $NaCoO_2$@GF/PVA-KOH/JC supercapacitor at specific currents ranging from 0.5 to 10 A g^{-1}. The tests were conducted within the same 1.7 V voltage range. Similar to the CV profiles, the GCD profiles exhibit two broad redox peaks at approximately ~0.6 V and ~1.2 V, reflecting the same redox processes observed in the CV analysis. Fig. 6(f) shows the Nyquist plot for the $NaCoO_2$@GF/PVA-KOH/JC supercapacitor device, along with its fitting curve. As with the previous Nyquist plot, the same electrical circuit model in Fig. 6(g) was employed to analyze the full cell configuration. In this model, the porous structure component represents the porous characteristics of both the positive and negative electrodes, while the active material component corresponds to the active sites of both electrodes. Using the same fitting procedure, the Nyquist plot for the $NaCoO_2$@GF/PVA-KOH/JC supercapacitor

device was fitted with remarkable accuracy, achieving a maximum average error of just 2%. The parameters obtained from the fitting procedure are presented in Table 2.

Table 2. Extracted parameters of the electrical circuit model fitting for the full cell configuration of the supercapacitor device

Electrode	R_s (Ohm)	R_{ct} (Ohm)	R_p (Ohm)	n_{ct}	n_c	n_p
Before Stability	2.2	1.3	13.2	1.00	0.70	0.64
After Stability	1.0	1.6	90.3	1.00	0.99	0.68

Interestingly, the resistance of the bulk electrolyte solution decreases after cycling performance, likely due to an increase in the electrode's wettability following several charge-discharge cycles. However, this better electrode's wettability is accompanied by an increase in both charge transfer resistance and the resistance of the porous structure after completing the cycles, which correlates with a slight reduction in the capacity retention of the supercapacitor devices. In addition to the increase of both charge transfer resistance and the resistance of the porous structure, this decline in capacity can also be attributed to an increase in the exponential term of CPE_c (n_c), indicating that the charge storage mechanism of the active material has shifted to being more capacitive than a combination of diffusive and capacitive mechanisms. This shift is noteworthy because a combination of these mechanisms is generally desired; the diffusive mechanism provides higher energy density, while the capacitive mechanism enhances power density—goals that hybrid supercapacitors aim to achieve. Overall, the fitting results from the Nyquist plot of the $NaCoO_2$@GF/PVA-KOH/JC supercapacitor reinforce the findings from the

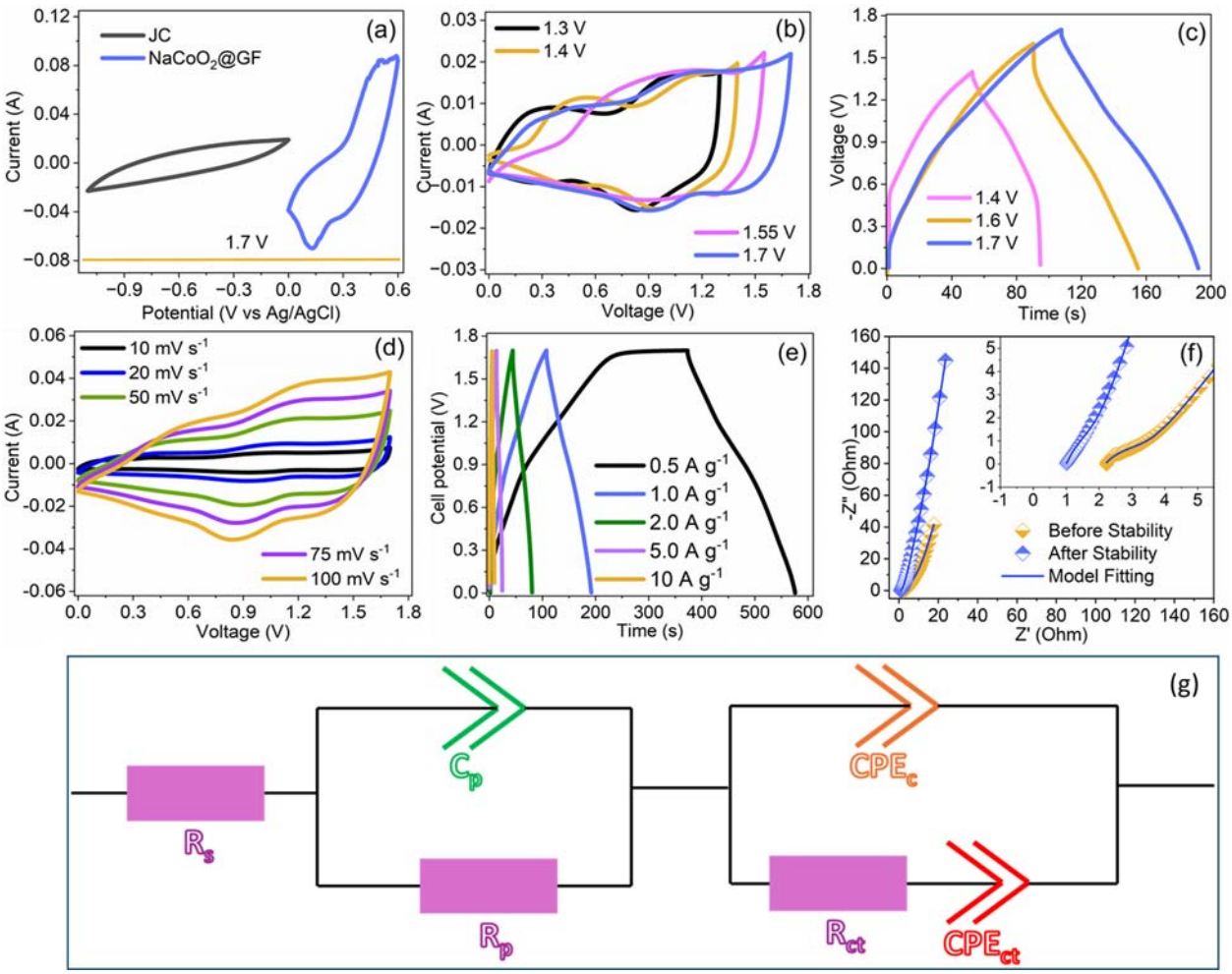

Fig. 6. (a) CV profiles of JC and $NaCoO_2$@GF composite with PVA-KOH polymer electrolyte in a half cell configuration, (b, c) CV and GCD profiles of $NaCoO_2$@GF/PVA-KOH/JC supercapacitor a symmetric device at different voltages, (d, e) CV and GCD profiles of $NaCoO_2$@GF/PVA-KOH/JC supercapacitor symmetric device at different scan rates and different current densities, (f) Experimental and model fitting EIS data of $NaCoO_2$@GF/PVA-KOH/JC supercapacitor device before and after stability and (g) Equivalent circuit used for fitting the EIS data in (f).

The specific capacitances were derived from the GCD profiles using equation 1. The specific capacitances were calculated to be 32.4, 28, 25, 21 and 17 F g^{-1} at 0.5, 1, 2, 5 and 10 A g^{-1}, respectively. These values are presented in the bar chart in Fig. 7(a). Thus, the CV and GCD analyses of the $NaCoO_2$@GF/PVA-KOH/JC full-cell supercapacitor demonstrate its robust

performance across a wide cell potential range of 0 to 1.7 V. The CV profiles reveal consistent behavior at various scan rates, indicating good material reversibility and efficient charge storage through surface redox reactions. The GCD profiles, which mirror the CV findings, further corroborate the device's capability, showing notable specific capacitance at different specific currents. The observed redox peaks in both analyses highlight the involvement of $Co^{2+} \leftrightarrow Co^{3+}$ redox reactions, essential for the device's energy storage mechanisms. The specific capacities derived from the GCD data underscore the device's potential for high-performance applications. Fig. 7(b) presents a double-Y plot displaying the Coulombic efficiency and retention of the $NaCoO_2$@GF/PVA-KOH/JC supercapacitor device. The Coulombic efficiency of the supercapacitor device remains close to 100% throughout 10,000 cycles. This high efficiency indicates minimal energy loss during the charge-discharge process, signifying excellent reversibility and low internal resistance. Initially, the retention increases gradually, reaching approximately 87% after 2,000 cycles. This initial rise can be attributed to the activation stage, during which the active sites of the electrode materials become fully accessible, enhancing the device's performance. The device maintains a retention level of around 87% throughout 6,000 cycles. This stability indicates the electrode materials' robustness and the electrolyte's effectiveness in maintaining performance over time. After 6,000 cycles, the retention drops slightly to about 83%, remaining consistent up to 10,000 cycles. This minor decrease suggests some degree of degradation of active material, which is typical in long-term cycling but still reflects impressive stability. The remarkable stability performance of the $NaCoO_2$@GF/PVA-KOH/JC supercapacitor device is attributed to the synergistic integration between the materials: On one side, the combination of GF (graphene foam) and $NaCoO_2$ provides a stable and conductive framework that supports efficient electron and ion transport. On the other side, the interaction between $NaCoO_2$ and JC (jute carbon) ensures a strong electrochemical relationship, enhancing the overall stability and performance of the device. Furthermore, the PVA-KOH gel polymer electrolyte provides a much higher ion conductivity in water solution. As a result, the $NaCoO_2$@GF/PVA-KOH/JC supercapacitor device demonstrates exceptional stability, as evidenced by its high Coulombic efficiency and retention over 10,000 cycles. The slight initial increase in retention during the activation stage and the minor drop after 6,000 cycles highlight the device's capacity to maintain performance over

extended use. The synergistic integration between GF, $NaCoO_2$, and JC is crucial in achieving this stability, ensuring efficient charge storage and long-term durability. This makes the $NaCoO_2$@GF/PVA-KOH/JC supercapacitor a promising candidate for practical energy storage applications where long cycle life and high efficiency are essential.

The power rule analysis and Dunn method were employed to analyze the energy storage mechanism of the $NaCoO_2$@GF/PVA-KOH/JC supercapacitor device, using equations (7) and (8). The anodic (positive scan rate) and cathodic (negative scan rate) peaks exhibit b-values of 0.88 and 0.91, respectively, as shown in Fig. 7(c). These similar values suggest that the energy storage mechanisms for both charging (anodic) and discharging (cathodic) are nearly reversible, which is beneficial for electrochemical devices. Fig. 7(d) presents the results from the Dunn method, indicating that the $NaCoO_2$@GF/PVA-KOH/JC device demonstrates a significant capacitive contribution, starting at 63% at 10 mV/s and increasing to 84% at 100 mV s^{-1}. This increase in capacitive contribution with higher scan rates is typical, as the capacitive mechanism becomes more dominant at faster rates. Additionally, Fig. (b) shows the energy storage mechanism, where, at a scan rate of 50 mV s^{-1}, 79% of the area under the CV curve is attributed to the capacitive contribution.

Moreover, the $NaCoO_2$@GF/PVA-KOH/JC supercapacitor delivers specific energy values of 36.2, 32.8, 31.4, 29.0, and 11.1 Wh kg^{-1} at specific currents of 0.5, 1, 2, 5, and 10 A g^{-1}, respectively as demonstrated in the Ragone plot in Fig. 7(f). Correspondingly, the specific power values are 627.5, 1325.4, 2766.9, 6314.6, and 7749.2 W kg^{-1} at the same current densities. The supercapacitor shows higher specific energy values at lower current densities (0.5 to 2 A g^{-1}), which indicates good energy storage capability. The specific energy decreases as the specific current increases, which is typical as higher current densities result in faster discharge rates and thus reduce the energy stored. The specific power values are significantly higher at higher current densities (5 to 10 A g^{-1}). This suggests that the supercapacitor can quickly deliver a large amount of power, which is advantageous for applications requiring rapid discharge. The specific energy and specific power values of the $NaCoO_2$@GF/PVA-KOH/JC supercapacitor are reported to be higher or in the same range as those found in the literature. This indicates that the device performs competitively compared to other supercapacitors reported in previous studies. This

means the Ragone plot in Fig. 7(f) demonstrates that the $NaCoO_2$@GF/PVA-KOH/JC supercapacitor excels in both specific energy and specific power, showing high performance across a range of current densities. Its specific energy is relatively high at lower current densities, while its specific power is impressive at higher current densities, aligning well with or surpassing other results in the literature. This suggests that the supercapacitor device offers a good balance between energy storage and power delivery, making it a strong candidate for applications that require both high and high-power densities.

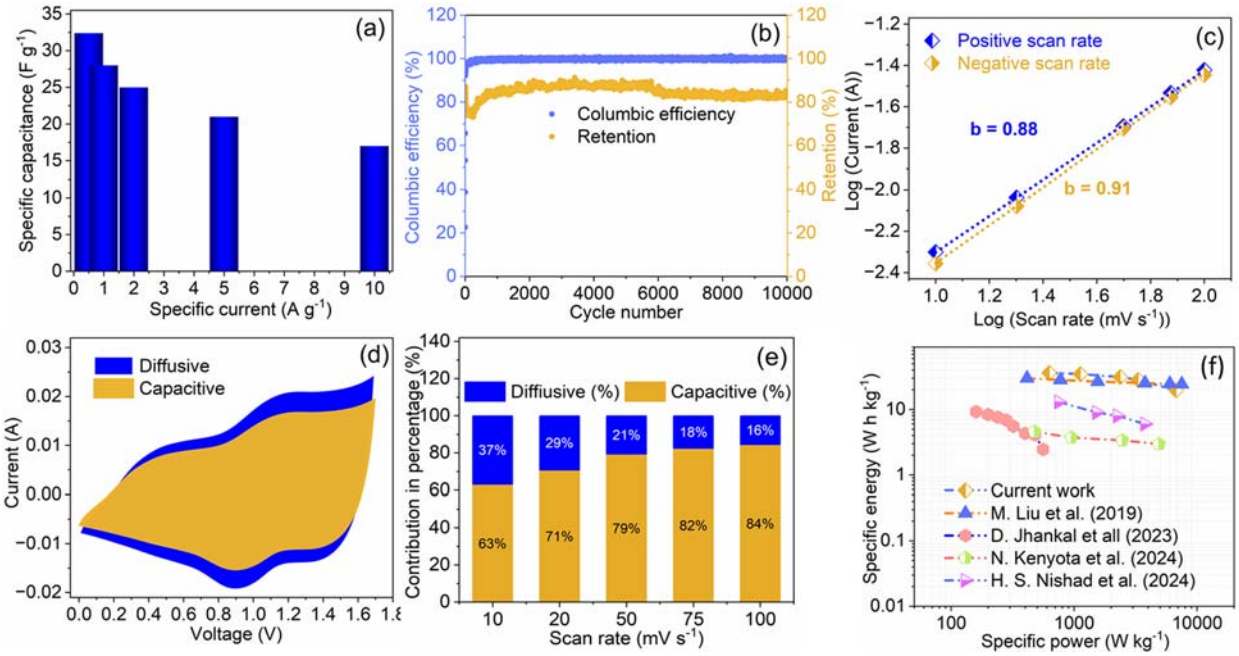

Fig. 7. (a) Specific capacitance of $NaCoO_2$@GF//JC supercapacitor device calculated at different specific currents, (b) Double-Y plot represents stability test of $NaCoO_2$@GF/PVA-KOH/JC supercapacitor device, (c) Power rule analysis of $NaCoO_2$@GF/PVA-KOH/JC supercapacitor device (d) The CV curve of $NaCoO_2$@GF/PVA-KOH/JC supercapacitor device with 79% of the area assigned to the capacitive mechanism contribution (e) The proportion of capacitive and diffusive contributions in CV at different scan rates examined for $NaCoO_2$@GF/PVA-KOH/JC supercapacitor device (f) Ragone plot of $NaCoO_2$@GF/PVA-KOH/JC supercapacitor device compared to similar devices from the literature [39][40][41][42].

Fig. 8 provides an analysis of the practical application of $NaCoO_2$@GF/PVA-KOH/JC supercapacitor device. It demonstrates the supercapacitor's ability to power an LED under different lighting conditions: in a lit room and a dark room. The analysis offers insights into the device's performance and energy delivery efficiency. Before testing the LED activation, the $NaCoO_2$@GF/PVA-KOH/JC supercapacitor was charged to its maximum voltage. In the beginning (Fig. 8(a)), the LED shows high intensity, indicating effective energy transfer from the fully charged supercapacitor device. This initial brightness reflects the supercapacitor's ability to deliver power immediately upon activation. After one minute (Fig. 8(b)), the LED's intensity remains strong but shows a slight reduction in brightness. This suggests that while the supercapacitor continues to supply power efficiently, the stored energy is beginning to deplete. By the five-minute mark, as shown in Fig. 8(c), the LED exhibits a noticeable decrease in brightness compared to earlier observations. However, it remains adequately lit, demonstrating that the $NaCoO_2$@GF/PVA-KOH/JC supercapacitor can sustain energy delivery for a reasonable duration. In the dark room, the initial intensity of the LED at 0 minutes is very high, showcasing the supercapacitor's ability to provide significant illumination as revealed in Fig. 8(d). The LED continues to shine brightly at 1 minute, although a slight decrease in intensity indicates ongoing energy consumption from the supercapacitor. As time progresses to 2, 3, 4, and 5 minutes, the intensity gradually decreases, yet the LED remains illuminated. This gradual decline indicates that while the supercapacitor is depleting its stored energy, it can still provide a reasonable level of brightness in a dark environment. Hence, this analysis demonstrates that the $NaCoO_2$@GF/PVA-KOH/JC supercapacitor can maintain adequate brightness over time, illustrating its potential for practical applications in energy storage and delivery. The performance characteristics observed in this work underscore the supercapacitor's efficiency, making it a promising candidate for future energy solutions.

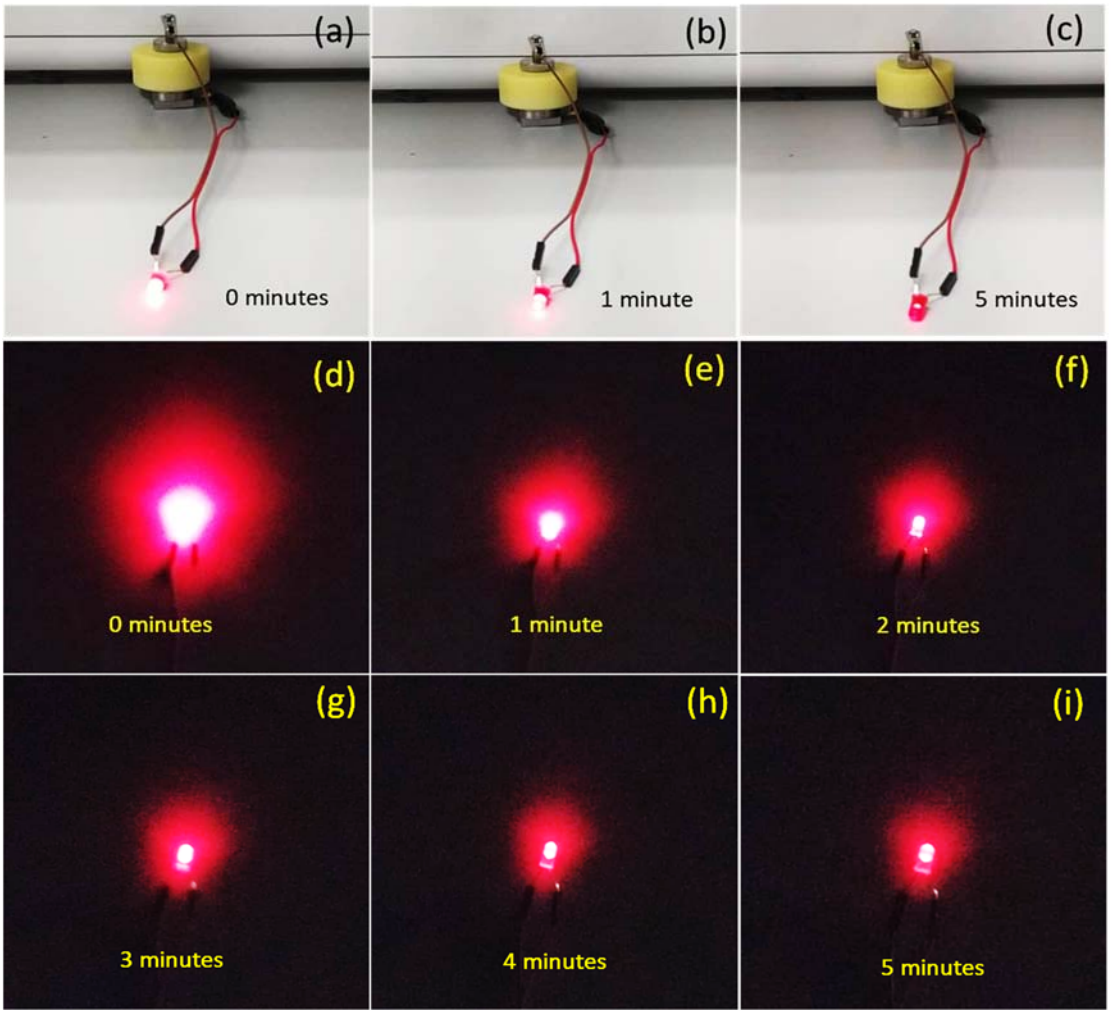

Fig. 8. LED activation in a lit room at (a) 0 min, (b) 1 min, and (c) 3 min, and in a dark room at (d) 0 min, (e) 1 min, (f) 2 min, (g) 3 min, (h) 4 min, and (i) 5 min.

4. CONCLUSION

In summary, this study successfully produced $NaCoO_2$@GF using a simple hydrothermal method. The successful integration of graphene foam (GF) into the $NaCoO_2$ matrix was further confirmed through different analyses. The conductive GF network facilitated efficient electron transfer and provided mechanical stability, while the $NaCoO_2$ redox-active material contributed to a high specific capacitance. Subsequently, $NaCoO_2$@GF/PVA-KOH/JC full asymmetric supercapacitor device was able to operate at a voltage of 1.7 V More significantly, the supercapacitor device demonstrated impressive electrochemical metrics, including specific energy values up to 36.2 Wh kg^{-1} at 0.5 A g^{-1}, and specific power values up to 7749.2 W kg^{-1} at 10 A g^{-1}. These performance

values are comparable to or even superior to those reported for some cobalt/sodium oxide-based materials in existing literature. Overall, the successful synthesis of the $NaCoO_2$@GF composite and its use in a high-performance supercapacitor device demonstrates the potential of this material for advanced energy storage applications.

Acknowledgements

The funding support provided by the Interdisciplinary Research Center for Hydrogen Technologies and Carbon Management (IRC-HTCM), King Fahd University of Petroleum & Minerals, Saudi Arabia, through the project INHE-22311 is greatly acknowledged.

References

[1] Conway, Brian E. Electrochemical supercapacitors: scientific fundamentals and technological applications. Springer Science & Business Media, 2013.

[2] P. Simon, Y. Gogotsi, N. Materials, Materials for electrochemical capacitors, Nature materials, 7(2008), 845-854.

[3] A. Muzaffar, M.B. Ahamed, C. Mustansar, Green supercapacitors : Latest developments and perspectives in the pursuit of sustainability, Renew. Sustain. Energy Rev. 195 (2024) 114324.

[4] C. Yuan, H. Xu, S.A. El-khodary, G. Ni, S. Esakkimuthu, S. Zhong, S. Wang, Recent advances and challenges in biomass-derived carbon materials for supercapacitors : A review, Fuel. 362 (2024) 130795.

[5] C. Xiong, T. Wang, Z. Zhao, Y. Ni, Recent progress in the development of smart supercapacitors, SmartMat. 4 (2023) e1158.

[6] J.R. Miller, P. Simon, Materials science: Electrochemical capacitors for energy management, Science. 321 (2008) 651–652.

[7] Y. Gogotsi, P. Simon, True performance metrics in electrochemical energy storage,

Science. 334 (2011) 917–918.

[8] A.G. Olabi, Q. Abbas, A. Al Makky, M.A. Abdelkareem, Supercapacitors as next generation energy storage devices: Properties and applications, Energy. 248 (2022) 123617.

[9] K.K. Patel, T. Singhal, V. Pandey, T.P. Sumangala, M.S. Sreekanth, Evolution and recent developments of high performance electrode material for supercapacitors: A review, J. Energy Storage. 44 (2021) 103366.

[10] L. Phor, A. Kumar, S. Chahal, Electrode materials for supercapacitors : A comprehensive review of advancements and performance, J. Energy Storage. 84 (2024) 110698.

[11] Z. Dai, U. Mani, H.T. Tan, Q. Yan, Advanced Cathode Materials for Sodium-Ion Batteries: What Determines Our Choices?, Small Methods. 1 (2017) 1–26.

[12] A.A. Mirghni, K.O. Oyedotun, O. Olaniyan, B.A. Mahmoud, N.F. Sylla, N. Manyala, Electrochemical analysis of Na-Ni bimetallic phosphate electrodes for supercapacitor applications, RSC Adv. 9 (2019) 25012-25021.

[13] S. Liu, L. Kang, J. Zhang, S.C. Jun, Y. Yamauchi, Sodium preintercalation-induced oxygen-deficient hydrated potassium manganese oxide for high-energy flexible Mg-ion supercapacitors, NPG Asia Mater. 15 (2023). 41427.

[14] P. Gaikwad, N. Tiwari, R. Kamat, S.M. Mane, S.B. Kulkarni, A comprehensive review on the progress of transition metal oxides materials as a supercapacitor electrode, Mater. Sci. Eng. B. 307 (2024) 117544.

[15] A.A. Mirghni, K.O. Oyedotun, B.A. Mahmoud, A. Bello, S.C. Ray, N. Manyala, Nickel-cobalt phosphate/graphene foam as enhanced electrode for hybrid supercapacitor, Compos. Part B Eng. 174 (2019) 106953.

[16] D.J. Tarimo, K.O. Oyedotun, A.A. Mirghni, B. Mutuma, N.F. Sylla, P. Murovhi, N. Manyala, Enhanced electrochemical performance of supercapattery derived from sulphur-reduced graphene oxide/cobalt oxide composite and activated carbon from peanut shells, Int. J. Hydrogen Energy. 45.58 (2020): 33059-33075.

[17] Q. Dai, Z. Zhao, M. Shi, C. Deng, H. Zhang, X. Li, Ion conductive membranes for flow batteries: Design and ions transport mechanism, J. Memb. Sci. 632 (2021) 119355.

[18] M. Kamal, J. Jaafar, A.A. Khan, Z. Khan, A.F. Ismail, M.H.D. Othman, M.A. Rahman, F. Aziz, G.U. Rehman, A Critical Review of the Advancement Approach and Strategy in SPEEK-Based Polymer Electrolyte Membrane for Hydrogen Fuel Cell Application, Energy and Fuels. 38 (2024) 12337–12386.

[19] M. Hina, S. Bashir, K. Kamran, F. Almomani, J. Ahmad, F. Kamarulazam, S. Ramesh, K. Ramesh, M.A. Mujtaba, Energy storage devices based on flexible and self-healable hydrogel electrolytes: Recent advances and future prospects, J. Energy Storage. 85 (2024) 110961.

[20] S. Alipoori, S. Mazinani, S.H. Aboutalebi, F. Sharif, Review of PVA-based gel polymer electrolytes in flexible solid-state supercapacitors: Opportunities and challenges, J. Energy Storage. 27 (2020) 101072.

[21] J.Y. Lee, J. Moon, C.S. Lee, J.T. Park, Improved polymer chain movement in Poly(Vinyl Alcohol)–Potassium hydroxide gel polymer electrolytes with nanostructured Cobalt(II,III) oxide fillers for supercapacitor, Mater. Today Chem. 33 (2023) 101740.

[22] S.I. Basha, A. Aziz, M. Maslehuddin, S. Ahmad, Preparation , Characterization , and Evaluation of the Anticorrosion Performance of Submicron / Nanocarbon from Jute, Chemistry–An Asian Journal 16.23 (2021): 3914-3930.

[23] S.S. Shah, E. Cevik, M.A. Aziz, T.F. Qahtan, A. Bozkurt, Z.H. Yamani, Jute Sticks Derived and Commercially Available Activated Carbons for Symmetric Supercapacitors with Bio-electrolyte: A Comparative Study, Synth. Met. 277 (2021) 116765.

[24] A.A. Mirghni, D. Momodu, K.O. Oyedotun, J.K. Dangbegnon, N. Manyala, Electrochemical analysis of $Co_3(PO4)_2{\cdot}4H_2O$/graphene foam composite for enhanced capacity and long cycle life hybrid asymmetric capacitors, Electrochim. Acta. 283 (2018) 374–384.

[25] M. Blangero, D. Carlier, M. Pollet, J. Darriet, C. Delmas, J.P. Doumerc, High-temperature

phase transition in the three-layered sodium cobaltite P' 3 -Na_x CoO_2 (x∼0.62), Phys. Rev. B - Condens. Matter Mater. Phys. 77 (2008) 0–8.

[26] K. Hirooka, O. Ichihashi, T. Takeguchi, Sodium cobalt oxide as a non-platinum cathode catalyst for microbial fuel cells, Sustain. Environ. Res. 28 (2018) 322–325.

[27] Q.H. Wu, A. Thißen, W. Jaegermann, XPS and UPS study of Na deposition on thin film V_2 O_5, Appl. Surf. Sci. 252 (2005) 1801–1805.

[28] S. Doubaji, B. Philippe, I. Saadoune, M. Gorgoi, T. Gustafsson, A. Solhy, M. Valvo, K. Edström, Passivation Layer and Cathodic Redox Reactions in Sodium-Ion Batteries Probed by HAXPES, ChemSusChem. 9 (2016) 97–108.

[29] Y. Lykhach, S. Piccinin, T. Skála, M. Bertram, N. Tsud, O. Brummel, M. Farnesi Camellone, K. Beranová, A. Neitzel, S. Fabris, K.C. Prince, V. Matolín, J. Libuda, Quantitative Analysis of the Oxidation State of Cobalt Oxides by Resonant Photoemission Spectroscopy, J. Phys. Chem. Lett. 10 (2019) 6129–6136.

[30] G.S. Jang, S. Ameen, M.S. Akhtar, H.S. Shin, Cobalt oxide nanocubes as electrode material for the performance evaluation of electrochemical supercapacitor, Ceram. Int. 44 (2018) 588–595.

[31] C. Bathula, I. Rabani, S. Ramesh, S.H. Lee, R.R. Palem, A.T.A. Ahmed, H.S. Kim, Y.S. Seo, H.S. Kim, Highly efficient solid-state synthesis of Co3O4 on multiwalled carbon nanotubes for supercapacitors, J. Alloys Compd. 887 (2021) 161307.

[32] A.A. Mirghni, M.J. Madito, K.O. Oyedotun, T.M. Masikhwa, N.M. Ndiaye, S.J. Ray, N. Manyala, A high energy density asymmetric supercapacitor utilizing a nickel phosphate/graphene foam composite as the cathode and carbonized iron cations adsorbed onto polyaniline as the anode, RSC Adv. 21 (2018) 11608-11621..

[33] V.A. Nebol'sin, V. Galstyan, Y.E. Silina, Graphene oxide and its chemical nature: Multi-stage interactions between the oxygen and graphene, Surfaces and Interfaces 21 (2020) 100763.

[34] A.G. Olabi, M.A. Abdelkareem, T. Wilberforce, E.T. Sayed, Application of graphene in energy storage device – A review, Renew. Sustain. Energy Rev. 135 (2021) 110026.

[35] R. Raccichini, A. Varzi, S. Passerini, B. Scrosati, The role of graphene for electrochemical energy storage, Nat. Mater. 14 (2015) 271–279.

[36] M.M. Mohamed, Y.P. Hardianto, A. Hussain, S.A. Ganiyu, M.A. Gondal, M.A. Aziz, Laser modified MnO2 cathode for augmented performance aqueous zinc ion batteries, Appl. Surf. Sci. 669 (2024) 160472.

[37] M.M. Mohamed, S.S. Shah, Y.P. Hardianto, A. Hussain, M.A. Gondal, M.A. Aziz, Pulsed laser-modified zinc anode with improved dendrite and corrosion resistance for sustainable high performance zinc ion hybrid supercapacitors, Mater. Chem. Phys. 326 (2024) 129809.

[38] M.M. Mohamed, M.A. Aziz, A. Hussain, Y.P. Hardianto, Z.H. Yamani, Dendrite-free zinc-ion hybrid supercapacitor with jute-derived carbon and nanostructured zinc on steel mesh for EVs, J. Energy Storage. 100 (2024) 113635.

[39] M. Liu, N. Shang, X. Zhang, S. Gao, C. Wang, Z. Wang, Microwave synthesis of sodium nickel-cobalt phosphates as high-performance electrode materials for supercapacitors, J. Alloys Compd. 791 (2019) 929–935.

[40] N. Kenyota, W. Jarernboon, P. Laokul, Bulk synthesis of chemically activated carbon and cobalt oxide nanocomposites as supercapacitor electrodes, J. Mater. Sci. Mater. Electron. 35 (2024) 1–22.

[41] H.S. Nishad, S.P. Gupta, V. Kotha, V. V. Magdum, V. V. Gawade, S.P. Patole, A. V. Biradar, P.S. Walke, Sodium-Substituted Tungsten Oxide Nanoflowers: An Efficient Electrode Enhancing the Pseudocapacitive Storage in Aqueous Asymmetric Supercapacitors, ChemNanoMat. 10 (2024) 1–8.

[42] D. Jhankal, M.S. Khan, P. Shakya, N. Bhardwaj, B. Yadav, K.K. Jhankal, K. Sachdev, Charge storage kinetics of interconnected MnO2 nano-needles/reduced graphene oxide

composite for high energy density quasi-solid-state sodium ion asymmetric supercapacitor, Energy Adv. 3 (2023) 191–202.